





In situ quantitative single-molecule study of dynamic catalytic processes in nanoconfinement

Bin Dong¹, Yuchen Pei², Fei Zhao¹, Tian Wei Goh¹, Zhiyuan Qi², Chaoxian Xiao², Kuangcai Chen¹,
Wenyu Huang¹^{2*} and Ning Fang¹^{*}

Understanding the fundamental catalytic principles when the catalytic centre is confined in nanoscale space that is dimensionally comparable to the reactant molecule is crucial for designing high-performance catalysts. Theoretical studies with simplified model systems and ensemble experimental measurements have shown that chemical reactions in nanoconfined environments are largely different from those in bulk solution. Here, we design a well-defined platform with catalytic centres confined in the end of nanopores with controlled lengths to study the in situ dynamic behaviour of catalytic processes under nanoconfinement at the single-molecule and single-particle level. Variable single molecular mass transport behaviour reveals the heterogeneity of the confined environment in the nanopores. With the capability of decoupling mass transport factors from reaction kinetics in the well-defined platform, we quantitatively uncovered a confinement-induced enhancement in the activity of platinum nanoparticles inside the nanopores. The combination of the unique model catalyst and the single-molecule super-localization imaging technique paves the way to understanding nanoconfinement effects in catalysis.

Molecules confined in nanoreactors—either synthetically generated or those native to biological structures—can bring significant changes to their physical and chemical properties. For example, the confinement can alter the Raman response of molecules in a single-wall carbon nanotube, the binding constant between ligands and receptors in a nanochannel, and the proton conductance inside a protein nanotube¹. In catalysis, nanoconfinement could dramatically change molecular transport and chemical conversion in porous materials, such as zeolites, mesoporous silica, carbon nanotubes and metal–organic frameworks. The importance of heterogeneous catalytic processes based on these porous materials demands a thorough understanding of the nanoconfinement effects for the rational design of high-efficiency catalysts. Theoretical studies using simplified model systems^{2–9}, along with ensemble experimental measurements^{10–21}, have led to a limited understanding of the confinement factors, including the size, shape and surface chemical properties of the pores on reaction kinetics. A significant breakthrough will be the development of single-molecule approaches to acquire direct experimental evidence and achieve quantitative understanding of the nanoconfinement effects at the single-molecule and single-nanopore level.

In the past decade, molecular diffusion in nanopores has been visualized at the single-molecule level^{22–27}, and single-turnover events on individual nanocatalysts such as layered double hydroxides²⁸, zeolites^{29–33}, metal nanoparticles (NPs)^{34–37} and semiconductors^{38–41} have been mapped with nanometre precision by super-resolution microscopy imaging. Furthermore, intraparticle diffusion-limited catalytic activity of porous materials^{42,43} has also recently been studied at the single-molecule level. However, the mass transport of reactant molecules and reaction kinetics of catalytic active sites in nanopores have never been measured together experimentally due to the seemingly insurmountable technical challenges of tracking single molecules dynamically in complex nanoporous structures under reaction conditions.

In the present study, a model nanocatalyst platform has been designed to enable the catalytic study of nanoconfinement effects at the single-molecule and single-particle level. After decoupling the mass transport factors from reaction kinetics, we quantitatively demonstrate the heterogeneous behaviour of single molecular mass transport confined in nanopores. Catalytic reaction rate and adsorption–desorption equilibrium constants were measured experimentally on the model nanocatalysts. The specially designed nanocatalysts are proven to be a versatile platform for future studies on different aspects of catalytic nanoconfinement effects, such as surface chemical properties and nanopore morphology.

Results

Design and characterization of the nanocatalyst platform. The nanocatalyst platform described in Fig. 1 has highly tunable structures with well-defined geometry and consists of platinum NPs sandwiched between an optically transparent solid SiO₂ core and a mesoporous SiO₂ shell (mSiO₂) with aligned nanopores. The synthesis of the nanocatalysts is discussed in detail in the Supplementary Methods. This nanocatalyst structure provides a restricted pathway for reactant molecules in the bulk solution to diffuse a uniform distance through the nanopores to access the active sites on confined platinum NPs placed at the bottom of the nanopores. Encapsulating platinum NPs in mSiO₂ shells provides many advantages, such as stabilizing the particle morphology and avoiding the aggregation of particles during the removal of surfactant ligands (Supplementary Figs. 2 and 3)⁴⁴. In the current experiments, the average diameter of the solid SiO₂ cores (105.0 ± 2.1 nm) and the thickness of the mSiO₂ shells (83.1 ± 9.0 nm and 118.5 ± 9.5 nm) were controlled (Supplementary Fig. 4) to keep all platinum NPs within the excitation depth (~300 nm) of total internal reflection fluorescence microscopy (Supplementary Fig. 5). The average diameter of the nanopores was measured as ~2.3 nm from the size distribution derived from the desorption branch using the Barret–Joyner–Halenda method and the cross-sectional profile in transmission electron microscopy

¹Department of Chemistry, Georgia State University, Atlanta, GA, USA. ²Department of Chemistry, Iowa State University, and Ames Laboratory, US Department of Energy, Ames, IA, USA. Bin Dong and Yuchen Pei contributed equally to this work. *e-mail: whuang@iastate.edu; nfang@gsu.edu

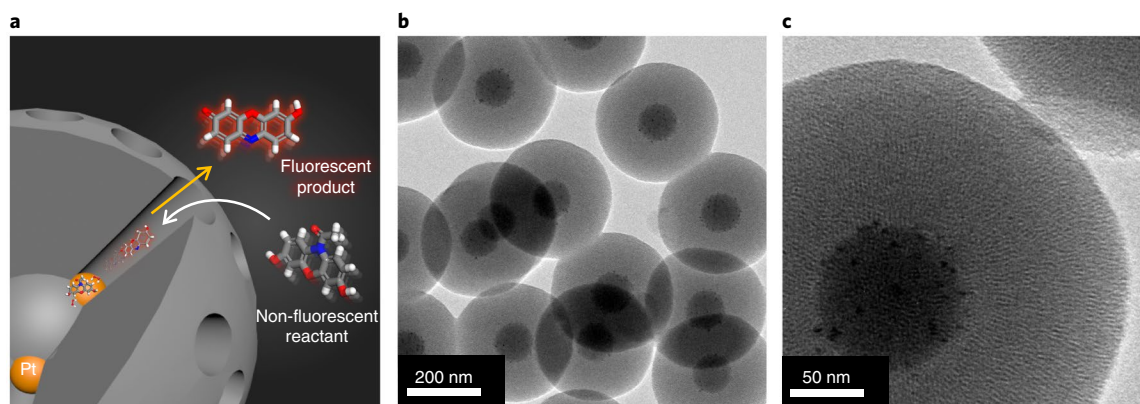


Fig. 1 | Multi-layer nanocatalysts as a model platform for simultaneously studying mass transport and heterogeneous surface catalysis. **a**, Scheme of the nanocatalyst that consists of 5 nm platinum NPs sandwiched between a solid 100 nm SiO₂ core and a mesoporous 120 nm mSiO₂ shell. **b,c**, Low-resolution (**b**) and high-resolution (**c**) transmission electron microscopy images of the as-synthesized nanocatalyst particles.

images of the nanocatalysts (Supplementary Figs. 6 and 7). The sandwiched platinum NPs had an average size (5.1 ± 1.0 nm) larger than the nanopore diameter and their locations were secured during the synthetic process and imaging experiments. We have experimentally verified that the reactant molecules have access throughout the nanopores (Supplementary Fig. 8). Thicker mesoporous shells were also prepared to validate the nanoconfinement effects through ensemble experiments (Supplementary Figs. 9–11).

Single-molecule fluorescence studies of the nanocatalyst. To study the in situ nanoconfinement effects on the catalytic activity,

we used a fluorogenic redox reaction as a probe (Supplementary Fig. 12). The non-fluorescent reactant molecule, amplex red, is oxidized by hydrogen peroxide at the surface active sites of platinum NPs to generate a highly fluorescent product molecule, resorufin. The fluorescence signal from resorufin was induced using a circularly polarized 532 nm laser with a total internal reflection fluorescence excitation scheme, collected using a high-numerical-aperture water immersion objective and imaged using a sensitive electron-multiplying charge-coupled device camera. Nanocatalysts were deposited on the surface of a quartz slide at a low density (Supplementary Fig. 13) to facilitate the study of individual

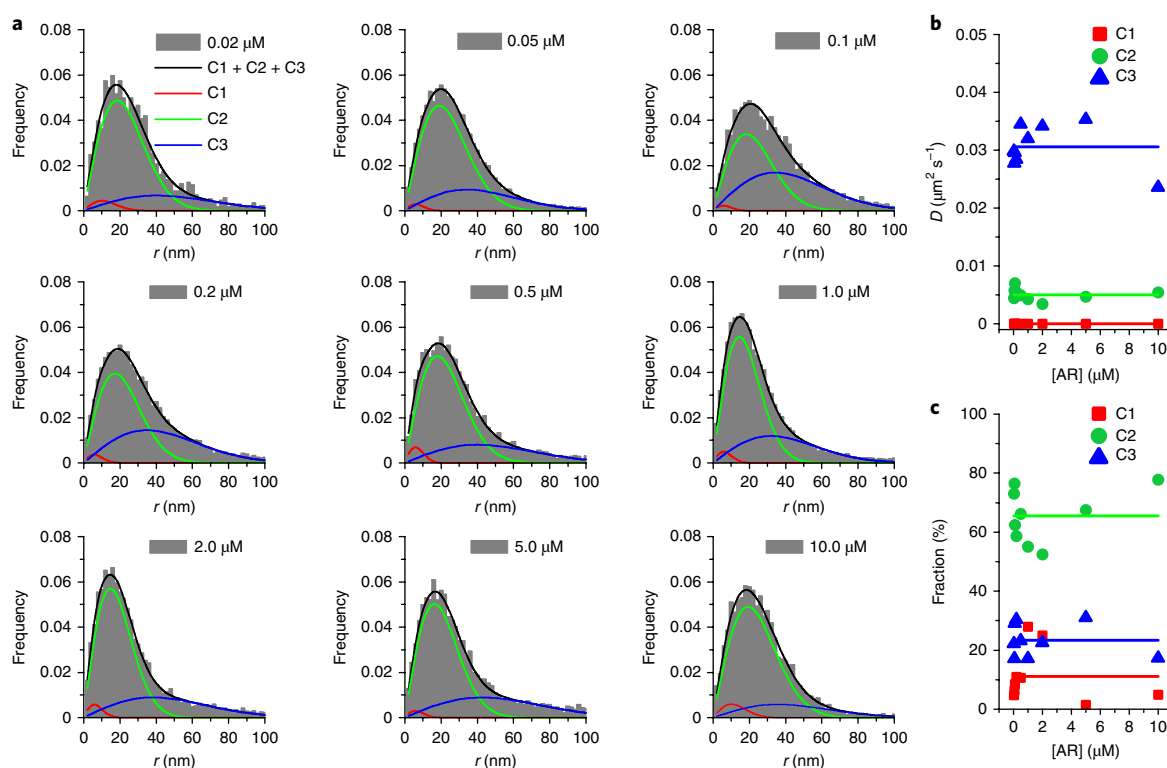


Fig. 2 | Diffusion coefficients of resorufin in 120-nm-long nanopores. **a**, Radial probability function for the distribution of the square root of resorufin diffusion's MSD in the nanopores. Three distinct characteristics 'r' were used in the fitting. **b,c**, Diffusion coefficients of resorufin (**b**) and their fractions (**c**) under different amplex red (AR) concentrations. The large variation of D indicates the heterogeneous properties of nanoporous materials.

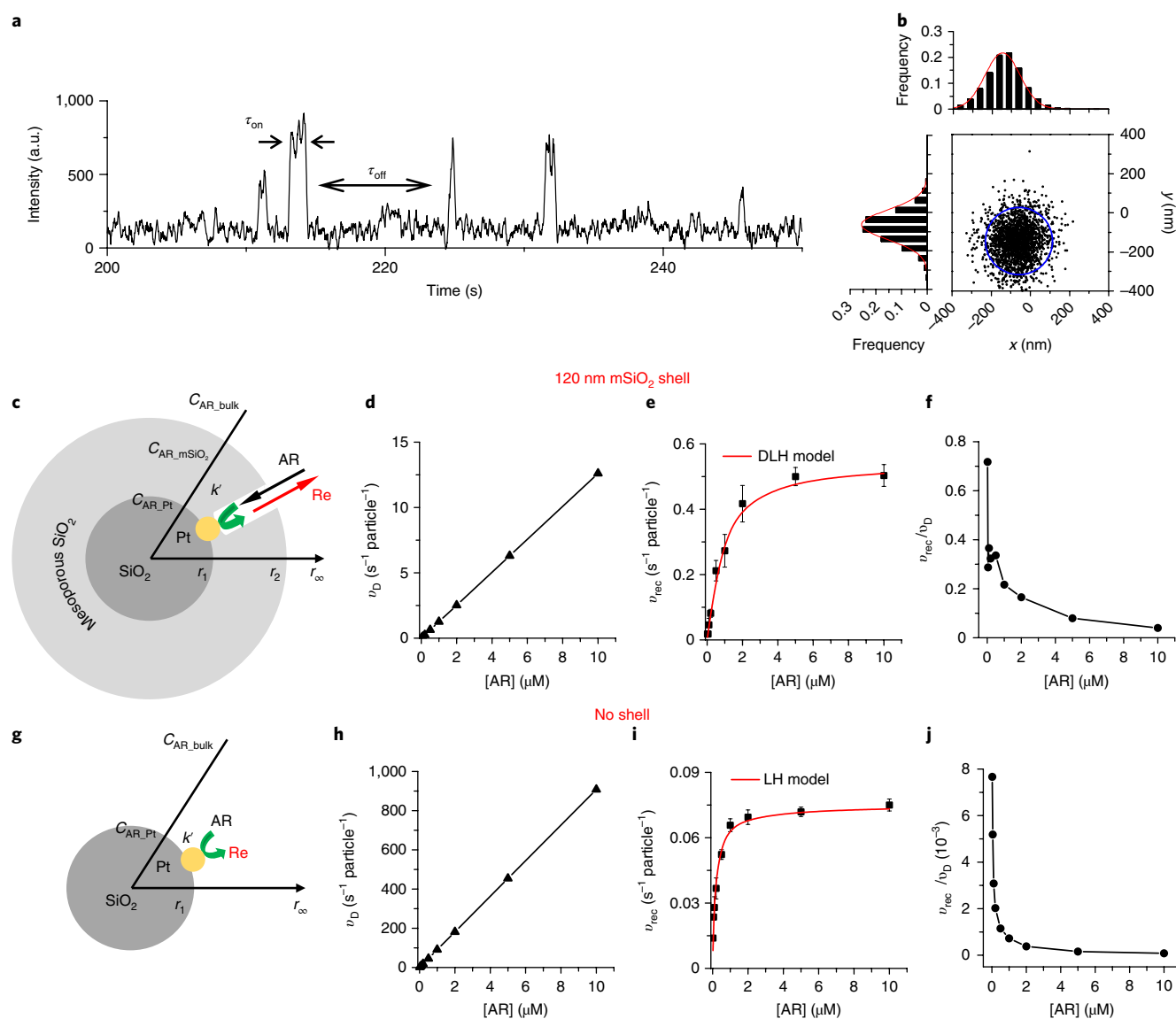


Fig. 3 | Catalytic activities at the single-molecule, single-particle level with turnover resolution. **a**, Segment of a typical fluorescence intensity trajectory from a single NP at a temporal resolution of 50 ms. τ_{on} and τ_{off} correspond to the resident time of resorufin in nanopores and the interval time between two consecutive catalytic events, respectively. **b**, Distribution of catalytic events on a nanocatalyst particle. **c–e**, Schematic model of the catalytic reaction in nanoconfinement (**c**), diffusion rate estimated from Fick's first law (**d**) and reaction kinetics measured from single-molecule, single-particle experiments of 100 nm SiO_2 @5 nm Pt@120 nm m SiO_2 (**e**). **f**, Ratio of the measured reaction rate over the diffusion rate. **g–j**, Same reaction kinetic study as in **c–f**, but performed on 100 nm SiO_2 @5 nm platinum. The error bars in **e** and **i** were calculated as the uncertainty of fitting the distribution of catalytic reaction rates from many (>60) nanocatalysts (Supplementary Fig. 22c). AR, amplex red; DLH, diffusion-limited Langmuir–Hinshelwood; Re, resorufin. $C_{\text{AR,bulk}}$, bulk concentration of AR; $C_{\text{AR,mSiO}_2}$, AR concentration near the nanopore entrance; $C_{\text{AR,Pt}}$, AR concentration near platinum NPs; v_D , diffusion rate of AR; v_{rec} , catalytic reaction rate of AR.

particles. A micro-flow system was used to supply a continuous flow of the reactant solution to maintain a constant and tunable concentration of amplex red outside the nanopores. Catalytic events were recorded and the positions of resorufin molecules in the nanopores were super-localized with nanometre-scale precision through point spread function fitting the single-molecule images (Supplementary Figs. 14 and 15). Scattering images were used to further identify the catalytic bursts on the nanocatalysts (Supplementary Fig. 16), with application of the sample stage drift correction (Supplementary Fig. 17) for extended experimental times.

Typical trajectories of fluorescent resorufin molecules diffusing through the nanopores before disappearing into the bulk solution were reconstructed (Supplementary Figs. 18 and 19). The results from the resorufin lifetime measurements (Supplementary Fig. 20)

confirmed that the resorufin fluorescence signal being extinguished was not caused by photobleaching. The diverse trajectories reflect the heterogeneity of the individual nanopores. To quantitatively describe the nanoconfinement effects on the mass transport of resorufin, over 10,000 single molecular trajectories were studied using mean squared displacement (MSD) analysis (Fig. 2 and Supplementary Figs. 18 and 19). To best interpret the MSD distributions, we fitted the data points with a radial probability density function to give three distinct characteristic diffusion coefficients (D) at $0.00006 \pm 0.00004 \mu\text{m}^2 \text{s}^{-1}$ ($11.2 \pm 9.2\%$, denoted as C1), $0.005 \pm 0.001 \mu\text{m}^2 \text{s}^{-1}$ ($65.5 \pm 9.2\%$, C2) and $0.031 \pm 0.004 \mu\text{m}^2 \text{s}^{-1}$ ($23.3 \pm 5.7\%$, C3). The distinct difference in the D values implies that the transport of resorufin in the nanopores should not be simply described as one Brownian motion, but rather as a combination

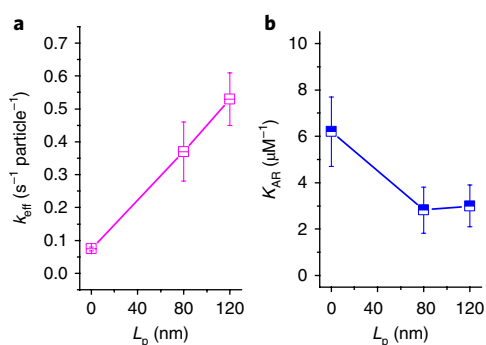


Fig. 4 | Quantitative comparison of nanoconfinement effects on the catalytic activities between non-confined and mSiO₂-confined platinum NPs. **a, b**, Catalytic reaction rate constant, k_{eff} (**a**) and adsorption-desorption equilibrium constant, K_{AR} (**b**) as a function of the mSiO₂ shell thickness (L_p). Nanocatalysts with platinum NPs confined within the mesoporous mSiO₂ shell (80 or 120 nm) provide higher k_{eff} but smaller K_{AR} than the platinum NPs without the mSiO₂ confinement. All error bars were calculated as the s.d. of the catalytic parameters (k_{eff} or K_{AR}) from many (>60) nanocatalysts.

of diffusion and adsorption behaviours associated with variable local environments. The medium diffusion rate (C2) is the dominant mode. However, the diffusion modes C1 and C3 are also observed in significant fractions, with C1 representing the adsorption of resorufin (where localization uncertainties dominate the measured MSD) and C3 representing the fast, random movement in the nanopores. To clearly distinguish moving molecules from adsorbed molecules in the MSD analysis, a control experiment was carried out with resorufin molecules immobilized on quartz slides (Supplementary Fig. 21). The variations in the measured positions of immobilized molecules, which were dominated by localization uncertainties, were indeed much smaller than those measured during catalysis.

The single molecular trajectory analysis provides accurate measurement of molecular diffusion in nanopores under reaction conditions²⁸, which then allows us to carry out further analysis to decouple the influence of molecular transport and reaction kinetics. In the remaining quantitative analysis, the apparent diffusion coefficient (D_{app} ; that is, the weighted average of C1, C2 and C3) of $0.011 \pm 0.003 \mu\text{m}^2 \text{s}^{-1}$ was used. It is clear that resorufin molecules diffuse at much slower speed in the nanopores compared with in the bulk solution ($D_{\text{bulk}} = 480 \mu\text{m}^2 \text{s}^{-1}$)⁴⁵. There are a few possible reasons for nanoconfinement effects that explain the much smaller diffusion rate of resorufin in the nanopores. First, the nanopore diameter (~2.3 nm) is comparable to the hydrodynamic size of resorufin (R_{H} , ~0.51 nm; Supplementary Note 1). Second, the viscosity of the medium has been reported to increase dramatically when confined in small space⁴⁶, which severely reduces the diffusion rate of trapped molecules. In this study, the viscosity of the medium (H₂O) inside the nanopores was estimated to be $67.6 \pm 8.4 \text{ Pa s}$ (Supplementary Note 2), which is around 4 orders of magnitude higher than that of normal aqueous solution (0.89 mPa s at 25 °C). Third, the adsorption of resorufin on the hydrophilic surface of the nanopores (silanol groups) also hinders the mass transport rate (Fig. 2, C1)²⁷.

Heterogeneous catalysis is an interplay between mass transport and chemical conversion, especially when catalytic centres are buried in porous materials such as the model system in this study. Using Fick's first law, the rate of amplex red diffusing onto the surface of platinum NPs was estimated to be 0.025 s^{-1} at $0.02 \mu\text{M}$ (the lowest concentration used in our experiments; Supplementary Note 3) of amplex red in the bulk solution (Fig. 3d). Even though

the structural effect in the mass transport of amplex red and resorufin cannot be completely ruled out, the diffusion coefficient of amplex red was assumed to be the same as that of resorufin to simplify the modelling parameters. From the experimental results (Fig. 3a,b), the single-particle reaction turnover rate was calculated to be $0.018 \pm 0.005 \text{ s}^{-1}$ using τ_{off}^{-1} (Supplementary Fig. 22) at $0.02 \mu\text{M}$ amplex red (Fig. 3e), where τ_{off} is the interval time between two consecutive catalytic events. This result clearly indicates that the reaction rate was mass transport limited at the very low concentration of amplex red. In contrast, a saturated reaction rate was achieved when the concentration of amplex red was much higher, where the mass transport rate was sufficiently large for the reaction rate to be limited solely by the chemical conversion rate (Fig. 3c–f). As a comparison, when nanoconfinement was not present (without the mSiO₂ shell), mass transport of amplex red played a negligible role in controlling the reaction rate (Fig. 3g–j).

Catalytic modelling of the nanoconfinement. Catalytic kinetics on the heterogeneous surface generally conforms to the Langmuir–Hinshelwood model when the reaction rate is purely chemical conversion limited. We fitted the kinetic data of a control sample without nanopores (100 nm SiO₂@ 5 nm platinum without mSiO₂ shells) with the Langmuir–Hinshelwood model in Fig. 3i. When there are no nanoconfinement effects on catalysis, it gives a chemical conversion rate constant of $k_{\text{eff}} = 0.074 \pm 0.006 \text{ s}^{-1} \text{ particle}^{-1}$ and an adsorption–desorption equilibrium constant $K_{\text{AR}} = 6.2 \pm 1.5 \mu\text{M}^{-1}$. However, the Langmuir–Hinshelwood model cannot be directly used to determine the chemical reaction kinetic parameters when nanoconfinement effects exist because mass transport plays an inevitable role in controlling the catalytic reaction rate (Supplementary Note 3). Herein, we established the diffusion-limited Langmuir–Hinshelwood kinetic model based on the steady-state assumption to correct the mass transport factor on measuring the chemical reaction kinetics when the catalytic reaction is affected by nanoconfinement (Supplementary Note 3). Fitting the reaction kinetics data in Fig. 3e with the diffusion-limited Langmuir–Hinshelwood model gives $k_{\text{eff}} = 0.53 \pm 0.08 \text{ s}^{-1} \text{ particle}^{-1}$ and $K_{\text{AR}} = 3.0 \pm 0.9 \mu\text{M}^{-1}$. These results show that k_{eff} increases by a factor of around seven, while K_{AR} is around two times smaller for platinum NPs confined in the nanopores (Fig. 4).

The enhanced activity of platinum NPs confined in the nanopores could be explained by either the increased effective concentration of amplex red in the nanoscale space⁷ or the nanoconfinement effect that helps to stabilize intermediate species or states⁹. Furthermore, the highly restricted space in the nanopores could constrain the molecular adsorption, thus decreasing the adsorption strength of amplex red. The heterogeneous catalytic activity enhances with an optimal adsorption strength of reactive species on the catalytic centres². The results here suggest that the nanoconfinement effects can potentially tune the adsorption strength of molecules.

Similar single-molecule and ensemble measurements were carried out on another nanocatalyst with the same design but a thinner shell thickness of ~80 nm. The measured D_{app} ($0.010 \pm 0.004 \mu\text{m}^2 \text{ s}^{-1}$) was virtually identical to the D_{app} for the 120 nm shell ($0.011 \pm 0.003 \mu\text{m}^2 \text{ s}^{-1}$), confirming that the diffusional behaviour of the tracked molecules was independent of the pore length. As shown in Fig. 4, K_{AR} values were also similar for both shell thicknesses, suggesting a similar adsorption–desorption strength of amplex red on platinum NPs in the nanopores with the same diameter and surface properties, but different pore lengths. Furthermore, k_{eff} for the 80 nm shell ($0.39 \pm 0.09 \text{ s}^{-1} \text{ particle}^{-1}$) was notably smaller than that for the 120 nm shell ($0.53 \pm 0.08 \text{ s}^{-1} \text{ particle}^{-1}$), which may be explained by the pore-length-dependent enhancement of the effective concentration of amplex red near platinum NPs. Ensemble measurements (Supplementary Fig. 23) also agree with the single-molecule data.

Nanoconfinement effects on catalytic processes are truly complicated and worth continued efforts to achieve a better understanding. The well-defined nanocatalysts used in the present study involve a multi-layered structure with which the composition, structure and surface properties of the solid core, aligned porous shell and sandwiched metal NPs can be customized independently. This provides us with a highly versatile platform for studying many aspects of nanoconfinement, especially pathway-dependent chemical processes and tandem reactions. For example, the catalytic effects of surface chemical properties (hydrophobic versus hydrophilic) and the nanopore morphology⁴³ (pore size, length and geometry) can be revealed in situ in the nanoscale-confined environment. This work paves the way for research to quantitatively differentiate, evaluate and understand the complex nanoconfinement effects on dynamic catalytic processes, thus guiding the rational design of high-performance catalysts.

Conclusion

A well-defined catalyst platform with nanoporous structures has been designed, which enables the quantitative study of the nanoconfinement effects in catalysis. A single-molecule, super-localization-based imaging technique was applied to reveal and differentiate the heterogeneous molecular transport and dynamic catalytic reaction kinetics in the nanopores at the single-molecule and single-particle turnover resolution under in situ conditions. The results show that the reaction rate is significantly increased in the presence of nanoconfinement, while the adsorption of reactant molecules on the surface of platinum NPs is weakened due to restricted molecular adsorption.

Methods

Catalyst preparation. The nanocatalysts were prepared by coating mesoporous silica shells on as-prepared platinum NP-loaded silica cores via the hydrolysis of tetraethyl orthosilicate in an ammonia–ethanol–water system. Hexadecyltrimethylammonium bromide was used as a pore-directing agent for the synthesis of mesoporous silica shells. A seeded growth method was used to ensure the uniformity of silica cores. Silica cores were functionalized with amino groups and further gently annealed before the loading of platinum NPs. Platinum NPs were synthesized by reducing K_2PtCl_4 in ethylene glycol with polyvinylpyrrolidone (molecular weight: 40,000) functioning as a capping agent.

Single-molecule fluorescence studies. The tracking and imaging of single-molecule transport was carried out using the total internal reflection fluorescence microscopy setup with an adjustable 50 mW/532 nm continuous wave laser (Uniphase), 60× water immersion objective (Olympus; numerical aperture: 1.2), iXonEM+ 897 camera (Andor Technology; 512×512 imaging array; 16 μm×16 μm pixel size) and fluorescence filter set composed of a 532 nm longpass filter, 532 nm notch filter and 568/40 bandpass filter (Semrock). A fluorogenic oxidation reaction of non-fluorescent amplex red (10-acetyl-3,7-dihydroxyphenoxazine) to produce highly fluorescent resorufin (maximum excitation wavelength, λ_{ex} = 563 nm and maximum emission wavelength, λ_{em} = 587 nm at pH 7.5) was used. A sample was typically prepared by spin-casting the nanocatalyst solution on a poly-L-lysine functionalized quartz slide. A steady stream of amplex red, H_2O_2 and pH 7.5 phosphate buffer mixture was introduced over the nanocatalysts using a syringe pump with a flow rate set to 10 μl min⁻¹.

Details of the synthesis of the nanocatalysts and the setup of the single-molecule fluorescence studies are included in the Supplementary Methods.

Data availability. All data are available from the corresponding authors upon reasonable request.

Received: 31 May 2017; Accepted: 13 December 2017;

Published online: 22 January 2018

References

- Petrosko, S. H., Johnson, R., White, H. & Mirkin, C. A. Nanoreactors: small spaces, big implications in chemistry. *J. Am. Chem. Soc.* **138**, 7443–7445 (2016).
- Yang, F., Deng, D., Pan, X., Fu, Q. & Bao, X. Understanding nano effects in catalysis. *Natl Sci. Rev.* **2**, 183–201 (2015).
- Lisal, M., Brennan, J. K. & Smith, W. R. Chemical reaction equilibrium in nanoporous materials: NO dimerization reaction in carbon slit nanopores. *J. Chem. Phys.* **124**, 64712 (2006).
- Jakobtorweihen, S., Hansen, N. & Keil, F. J. Combining reactive and configurational-bias Monte Carlo: confinement influence on the propene metathesis reaction system in various zeolites. *J. Chem. Phys.* **125**, 224709 (2006).
- Santiso, E. E., Kostov, M. K., George, A. M., Nardelli, M. B. & Gubbins, K. E. Confinement effects on chemical reactions—toward an integrated rational catalyst design. *Appl. Surf. Sci.* **253**, 5570–5579 (2007).
- Maličevský, A. & Lisal, M. Density functional study of chemical reaction equilibrium for dimerization reactions in slit and cylindrical nanopores. *J. Chem. Phys.* **130**, 164713 (2009).
- Santiso, E. E., George, A. M., Gubbins, K. E. & Nardelli, M. B. Effect of confinement by porous carbons on the unimolecular decomposition of formaldehyde. *J. Chem. Phys.* **125**, 084711 (2006).
- Hansen, N., Jakobtorweihen, S. & Keil, F. J. Reactive Monte Carlo and grand-canonical Monte Carlo simulations of the propene metathesis reaction system. *J. Chem. Phys.* **122**, 164705 (2005).
- Santiso, E. E., Nardelli, M. B. & Gubbins, K. E. A remarkable shape-catalytic effect of confinement on the rotational isomerization of small hydrocarbons. *J. Chem. Phys.* **128**, 034704 (2008).
- Xiao, J., Pan, X., Guo, S., Ren, P. & Bao, X. Toward fundamentals of confined catalysis in carbon nanotubes. *J. Am. Chem. Soc.* **137**, 477–482 (2015).
- Bae, J. H., Han, J.-H., Han, D. & Chung, T. D. Effects of adsorption and confinement on nanoporous electrochemistry. *Farad. Discuss.* **164**, 361–376 (2013).
- Bi, H., Qiao, L., Busnel, J.-M., Liu, B. & Girault, H. H. Kinetics of proteolytic reactions in nanoporous materials. *J. Proteome Res.* **8**, 4685–4692 (2009).
- Chen, P.-C. et al. Tip-directed synthesis of multimetallic nanoparticles. *J. Am. Chem. Soc.* **137**, 9167–9173 (2015).
- Deraedt, C. & Astruc, D. Supramolecular nanoreactors for catalysis. *Coord. Chem. Rev.* **324**, 106–122 (2016).
- Deraedt, C., Pinaud, N. & Astruc, D. Recyclable catalytic dendrimer nanoreactor for part-per-million CuI catalysis of “click” chemistry in water. *J. Am. Chem. Soc.* **136**, 12092–12098 (2014).
- Grochmal, A., Prout, L., Makin-Taylor, R., Prohens, R. & Tomas, S. Modulation of reactivity in the cavity of liposomes promotes the formation of peptide bonds. *J. Am. Chem. Soc.* **137**, 12269–12275 (2015).
- Li, G. et al. Giant Raman response to the encapsulation of sulfur in narrow diameter single-walled carbon nanotubes. *J. Am. Chem. Soc.* **138**, 40–43 (2016).
- Liu, H., Yu, H., Xiong, C. & Zhou, S. Architecture controlled PtNi@mSiO₂ and Pt–NiO@mSiO₂ mesoporous core–shell nanocatalysts for enhanced *p*-chloronitrobenzene hydrogenation selectivity. *RSC Adv.* **5**, 20238–20247 (2015).
- Tagliacozzi, M. & Szleifer, I. How does confinement change ligand–receptor binding equilibrium? Protein binding in nanopores and nanochannels. *J. Am. Chem. Soc.* **137**, 12539–12551 (2015).
- Zhai, B. et al. Enhanced hydrogen desorption properties of LiBH₄–Ca(BH₄)₂ by a synergetic effect of nanoconfinement and catalysis. *Int. J. Hydrog. Energy* **41**, 17462–17470 (2016).
- Zhao, H. et al. Reversible trapping and reaction acceleration within dynamically self-assembling nanoflasks. *Nat. Nanotech.* **11**, 82–88 (2016).
- Zurner, A., Kirstein, J., Doblinger, M., Bräuchle, C. & Bein, T. Visualizing single-molecule diffusion in mesoporous materials. *Nature* **450**, 705–708 (2007).
- Tran-Ba, K.-H., Finley, J. J., Higgins, D. A. & Ito, T. Single-molecule tracking studies of millimeter-scale cylindrical domain alignment in polystyrene–poly(ethylene oxide) diblock copolymer films induced by solvent vapor penetration. *J. Phys. Chem. Lett.* **3**, 1968–1973 (2012).
- Jung, C. et al. Diffusion of oriented single molecules with switchable mobility in networks of long unidimensional nanochannels. *J. Am. Chem. Soc.* **130**, 1638–1648 (2008).
- Feil, F., Cauda, V., Bein, T. & Bräuchle, C. Direct visualization of dye and oligonucleotide diffusion in silica filaments with collinear mesopores. *Nano Lett.* **12**, 1354–1361 (2012).
- Rühle, B., Davies, M., Lebold, T., Bräuchle, C. & Bein, T. Highly oriented mesoporous silica channels synthesized in microgrooves and visualized with single-molecule diffusion. *ACS Nano* **6**, 1948–1960 (2012).
- Lebold, T., Michaelis, J. & Bräuchle, C. The complexity of mesoporous silica nanomaterials unravelled by single molecule microscopy. *Phys. Chem. Chem. Phys.* **13**, 5017–5033 (2011).
- Roeffaers, M. B. J. et al. Spatially resolved observation of crystal-face-dependent catalysis by single turnover counting. *Nature* **439**, 572–575 (2006).
- Ristanović, Z. et al. Quantitative 3D fluorescence imaging of single catalytic turnovers reveals spatiotemporal gradients in reactivity of zeolite H-ZSM-5 crystals upon steaming. *J. Am. Chem. Soc.* **137**, 6559–6568 (2015).
- Ristanović, Z., Kubarev, A. V., Hofkens, J., Roeffaers, M. B. J. & Weckhuysen, B. M. Single molecule nanospectroscopy visualizes proton-transfer processes within a zeolite crystal. *J. Am. Chem. Soc.* **138**, 13586–13596 (2016).
- Roeffaers, M. B. J. et al. Super-resolution reactivity mapping of nanostructured catalyst particles. *Angew. Chem. Int. Ed.* **121**, 9449–9453 (2009).
- Ristanović, Z. et al. High-resolution single-molecule fluorescence imaging of zeolite aggregates within real-life fluid catalytic cracking particles. *Angew. Chem. Int. Ed.* **54**, 1836–1840 (2015).

33. Hendriks, F. C. et al. Single-molecule fluorescence microscopy reveals local diffusion coefficients in the pore network of an individual catalyst particle. *J. Am. Chem. Soc.* **139**, 13632–13635 (2017).
34. Zhou, X. et al. Quantitative super-resolution imaging uncovers reactivity patterns on single nanocatalysts. *Nat. Nanotech.* **7**, 237–241 (2012).
35. Han, K. S., Liu, G., Zhou, X., Medina, R. E. & Chen, P. How does a single Pt nanocatalyst behave in two different reactions? A single-molecule study. *Nano Lett.* **12**, 1253–1259 (2012).
36. Andoy, N. M. et al. Single-molecule catalysis mapping quantifies site-specific activity and uncovers radial activity gradient on single 2D nanocrystals. *J. Am. Chem. Soc.* **135**, 1845–1852 (2013).
37. Xu, W., Kong, J. S., Yeh, Y.-T. E. & Chen, P. Single-molecule nanocatalysis reveals heterogeneous reaction pathways and catalytic dynamics. *Nat. Mater.* **7**, 992–996 (2008).
38. Ha, J. W. et al. Super-resolution mapping of photogenerated electron and hole separation in single metal–semiconductor nanocatalysts. *J. Am. Chem. Soc.* **136**, 1398–1408 (2014).
39. Tachikawa, T., Yamashita, S. & Majima, T. Evidence for crystal-face-dependent TiO₂ photocatalysis from single-molecule imaging and kinetic analysis. *J. Am. Chem. Soc.* **133**, 7197–7204 (2011).
40. Sambur, J. B. et al. Sub-particle reaction and photocurrent mapping to optimize catalyst-modified photoanodes. *Nature* **530**, 77–80 (2016).
41. Sambur, J. B. & Chen, P. Distinguishing direct and indirect photoelectrocatalytic oxidation mechanisms using quantitative single-molecule reaction imaging and photocurrent measurements. *J. Phys. Chem. C* **120**, 20668–20676 (2016).
42. De Cremer, G. et al. High-resolution single-turnover mapping reveals intraparticle diffusion limitation in Ti–MCM-41-catalyzed epoxidation. *Angew. Chem. Int. Ed.* **122**, 920–923 (2010).
43. Kubarev, A. V., Janssen, K. P. F. & Roeloffs, M. B. J. Noninvasive nanoscopy uncovers the impact of the hierarchical porous structure on the catalytic activity of single dealuminated mordenite crystals. *ChemCatChem* **7**, 3646–3650 (2015).
44. Joo, S. H. et al. Thermally stable Pt/mesoporous silica core–shell nanocatalysts for high-temperature reactions. *Nat. Mater.* **8**, 126–131 (2009).
45. Schilling, E. A., Kamholz, A. E. & Yager, P. Cell lysis and protein extraction in a microfluidic device with detection by a fluorogenic enzyme assay. *Anal. Chem.* **74**, 1798–1804 (2002).
46. Li, L., Kazoe, Y., Mawatari, K., Sugii, Y. & Kitamori, T. Viscosity and wetting property of water confined in extended nanospace simultaneously measured from highly-pressurized meniscus motion. *J. Phys. Chem. Lett.* **3**, 2447–2452 (2012).

Acknowledgements

This work was supported by the National Science Foundation (CHE-1609225/1607305).

Author contributions

B.D., Y.P., W.H. and N.F. conceived the idea, designed the experiments and wrote the manuscript. B.D., F.Z., K.C. and N.F. performed the imaging experiments. Y.P., T.W.G., Z.Q., C.X. and W.H. performed the synthesis and characterization of the nanocatalysts.

Competing interests

The authors declare no competing financial interests.

Additional information

Supplementary information is available for this paper at <https://doi.org/10.1038/s41929-017-0021-1>.

Reprints and permissions information is available at www.nature.com/reprints.

Correspondence and requests for materials should be addressed to W.H. or N.F.

Publisher's note: Springer Nature remains neutral with regard to jurisdictional claims in published maps and institutional affiliations.